

# Analysis of long-lived effects in high-repetition-rate stroboscopic transient X-ray absorption experiments on thin films

TOBIAS LOJEWSKI,<sup>a\*</sup> LOIČ LE GUYADER,<sup>b</sup> NAMAN AGARWAL,<sup>b,c</sup>  
 CHRISTINE BOEGLIN,<sup>d</sup> ROBERT CARLEY,<sup>b</sup> ANDREA CASTOLDI,<sup>e,f</sup>  
 CARSTEN DEITER,<sup>b</sup> ROBIN Y. ENGEL,<sup>g</sup> FLORIAN ERDINGER,<sup>h,i</sup>  
 HANS FANGOHR,<sup>b,j,k</sup> CARLO FIORINI,<sup>l,m</sup> NATALIA GERASIMOVA,<sup>b</sup> RAFAEL GORT,<sup>b</sup>  
 FRANK DE GROOT,<sup>n</sup> KARSTEN HANSEN,<sup>b</sup> STEFFEN HAUF,<sup>b</sup> DAVID HICKIN,<sup>b</sup>  
 MANUEL IZQUIERDO,<sup>b</sup> LEA KÄMMERER,<sup>a</sup> BENJAMIN E. VAN KUIKEN,<sup>b</sup>  
 DAVID LOMIDZE,<sup>b</sup> STEFANO MAFFESSANTI,<sup>g</sup> LAURENT MERCADIER,<sup>b</sup>  
 GIUSEPPE MERCURIO,<sup>b</sup> PITER S. MIEDEMA,<sup>g</sup> MATTHIAS PACE,<sup>d</sup>  
 MATTEO PORRO,<sup>b,o</sup> JAVAD REZVANI,<sup>p</sup> NICO ROTHENBACH,<sup>a</sup> BENEDIKT RÖSNER,<sup>q</sup>  
 ANDREY SAMARTSEV,<sup>b,g</sup> JUSTINA SCHLAPPA,<sup>b</sup> CHRISTIAN STAMM,<sup>r,s</sup>  
 MARTIN TEICHMANN,<sup>b</sup> MONICA TURCATO,<sup>b</sup> ALEXANDER YAROSLAVTSEV,<sup>b,t</sup>  
 FLORIAN DÖRING,<sup>q</sup> ANDREAS SCHERZ,<sup>b</sup> CHRISTIAN DAVID,<sup>q</sup> MARTIN BEYE,<sup>g,u</sup>  
 UWE BOVENSIEPEN,<sup>a,v</sup> HEIKO WENDE,<sup>a</sup> ANDREA ESCHENLOHR<sup>a</sup> AND  
 KATHARINA OLLEFS<sup>a</sup>

<sup>a</sup>*Faculty of Physics and Center for Nanointegration Duisburg-Essen (CENIDE),  
 University of Duisburg-Essen, Lotharstr. 1, 47057 Duisburg, Germany,* <sup>b</sup>*European  
 XFEL, Holzkoppel 4, 22869 Schenefeld, Germany,* <sup>c</sup>*Elettra Sincrotrone Trieste,  
 Strada Statale 14 - km 163,5, 34149 Basovizza, Trieste, ITALY,* <sup>d</sup>*Université de  
 Strasbourg, CNRS, Institut de Physique et Chimie des Matériaux de Strasbourg,  
 UMR 7504, 67000 Strasbourg, France,* <sup>e</sup>*Dipartimento di Elettronica, Informazione e  
 Bioingegneria, Politecnico di Milano, 20133 Milano, Italy,* <sup>f</sup>*Istituto Nazionale di*

*Fisica Nucleare, Sez., Milano, 20133 Milano, Italy, <sup>g</sup>Deutsches Elektronen-Synchrotron DESY, Notkestr. 85, 22607 Hamburg, Germany, <sup>h</sup>EXTOLL GmbH, 68159 Mannheim, Germany, <sup>i</sup>Institute for Computer Engineering, University of Heidelberg, Im Neuenheimer Feld 368, 69120 Heidelberg, Germany, <sup>j</sup>Max-Planck Institute for the Structure and Dynamics of Matter, Luruper Chaussee 149, 22761 Hamburg, Germany, <sup>k</sup>University of Southampton, Southampton SO17 1BJ, United Kingdom, <sup>l</sup>Dipartimento di Elettronica, Informazione e Bioingegneria, Politecnico di Milano, 20133 Milano, Italy, <sup>m</sup>Istituto Nazionale di Fisica Nucleare, Sez., Milano, 20133 Milano, Italy, <sup>n</sup>Materials Chemistry and Catalysis (MCC), Debye Institute for Nanomaterials Science, Utrecht University, Universiteitslaan 99, 3584 CG, Utrecht, The Netherlands, <sup>o</sup>Department of Molecular Sciences and Nanosystems, Ca' Foscari University of Venice, 30172 Venezia, Italy, <sup>p</sup>Laboratori Nazionali di Frascati, INFN, Via Enrico Fermi 54, 00044 Frascati (Roma), Italy, <sup>q</sup>Paul Scherrer Institut, Forschungsstr. 111, 5232 Villigen PSI, Switzerland, <sup>r</sup>Department of Materials, ETH Zurich, 8093 Zurich, Switzerland, <sup>s</sup>Institute for Electric Power Systems, University of Applied Sciences and Arts Northwestern Switzerland, 5210 Windisch, Switzerland, <sup>t</sup>MAX IV Laboratory, Lund University, Box 118, 221 00 Lund, Sweden, <sup>u</sup>Department of Physics, AlbaNova University Center, Stockholm University, SE-10691 Stockholm, Sweden, and <sup>v</sup>Institute for Solid State Physics, The University of Tokyo, Kashiwa, Chiba 277-8581, Japan. E-mail: tobias.lojewski@uni-due.de*

## Abstract

Time-resolved X-ray absorption spectroscopy (tr-XAS) has been shown to be a versatile measurement technique for investigating non-equilibrium dynamics. Novel X-ray

free electron laser (XFEL) facilities like the European XFEL offer increased repetition rates for stroboscopic XAS experiments through a burst operation mode, which enables measurements with up to 4.5 MHz. These higher repetition rates lead to higher data acquisition rates but can also introduce long-lived excitations that persist and thus build up during each burst. Here, we report on such long-lived effects in Ni and NiO thin film samples that were measured at the European XFEL. We disentangle the long-lived excitations from the initial pump-induced change and perform a detailed modelling-based analysis of how they modify transient X-ray spectra. As a result, we link the long-lived effects in Ni to a local temperature increase, as well as the effects in NiO to excited charge carrier trapping through polaron formation. In addition, we present possible correction methods, as well as discuss ways in which the effects of these long-lived excitations could be minimized for future time-resolved X-ray absorption spectroscopy measurements.

## 1. Introduction

X-ray absorption spectroscopy (XAS) is a powerful measurement technique to examine the electronic and magnetic properties of condensed matter, providing element-specific information about the electronic structure, magnetic properties, and the chemical environment (Stöhr & Siegmann, 2006; Willmott, 2019). Due to the sensitivity to changes in the electronic structure and its element-specificity, XAS has been proven in recent years to be a great tool for investigating non-equilibrium states in condensed matter. Following an optical laser excitation of the sample, transient XAS can trace modifications of the electronic structure in time, as initially shown by Stamm *et al.* (Stamm *et al.*, 2007). Since then, femtosecond time-resolved soft X-ray absorption spectroscopy on thin-film samples has been used to investigate changes in the magnetization (Stamm *et al.*, 2007; Stamm *et al.*, 2010; López-Flores *et al.*, 2012; López-

Flores *et al.*, 2013; Hennecke *et al.*, 2019), the role of the lattice in the non-equilibrium energy transfer (Rothenbach *et al.*, 2019; Rothenbach *et al.*, 2021), photoexcitations in functional photocatalytic materials (Uemura *et al.*, 2021; Uemura *et al.*, 2022), and optically induced spin currents (Eschenlohr *et al.*, 2013; Eschenlohr *et al.*, 2017; Stamm *et al.*, 2020; Eschenlohr, 2021).

With transient X-ray absorption being a well-established and versatile measurement technique, the focus was directed towards improving the experimental setups in regard to energy-, time resolution, and measurement time. For stroboscopic-type experiments such as pump-probe XAS, the measurement time can be reduced by increasing the brilliance of the X-ray sources as well as the repetition rate, while the time resolution can be improved up to a certain point with short X-ray and laser pulses and a more stable temporal overlap. At third-generation synchrotron radiation facilities, pulse lengths are typically between 50 and 100 ps (Stepanov & Hauri, 2016). Using a laser-slicing-based technique, where only a small slice of electrons from the main electron bunch are modulated in energy, it is possible to reduce the pulse length to around 100 fs, but at the cost of the number of X-ray photons (Stepanov & Hauri, 2016; Holl-dack *et al.*, 2014). X-ray free electron lasers, on the other hand, offer inherently short X-ray flashes at around 100 fs with extremely high peak brilliances. However, facilities with a normal-conducting accelerator design have historically had reduced repetition rates of typically between 60 and 120 Hz (Stepanov & Hauri, 2016; Tschentscher *et al.*, 2017; Emma *et al.*, 2010; Ishikawa *et al.*, 2012; Ko *et al.*, 2017; Patterson *et al.*, 2010) compared to third-generation synchrotron sources. Facilities that employ a superconducting accelerator design (Decking *et al.*, 2020) are able to achieve comparatively higher repetition rates, such as FLASH, which can operate between 10 Hz and 5 kHz (Ackermann *et al.*, 2007; Allaria *et al.*, 2021), and the European XFEL which can reach up to 4.5 MHz (Stepanov & Hauri, 2016; Tschentscher *et al.*, 2017; Le Guyader

*et al.*, 2023). Typically, these repetition rates are achieved through a burst operation mode, with the exception of the currently ongoing LCLS-II upgrade, which is planning to achieve a 1 MHz repetition rate in continuous operation (Raubenheimer, 2018; Brachmann *et al.*, 2019). Specifically at the European XFEL, the repetition rate of 4.5 MHz is achieved in a burst operation mode where up to 2700 electron bunches are generated and accelerated in short bursts (intra-burst temporal spacing of 222 ns), with a burst repetition rate of 10 Hz. With these high repetition rates and the high peak brilliance, this setup enables extremely efficient data acquisition, which allows the focus to shift towards performing a time-resolved spectroscopic analysis of the pump-induced changes to disentangle the initial excitation and subsequent relaxation dynamics (Lojewski *et al.*, 2023; Lojewski *et al.*, 2024). However, high-repetition-rate stroboscopic experiments also bring additional challenges. Long-lived excitations, in this context defined as excitations that do not fully relax back to the initial ground state before the next optical excitation, can lead to a gradual modification of the pump-induced change over the course of the burst through the additional energy that is deposited with each subsequent excitation. One such effect is laser-induced heating, which was already observed in transient XAS experiments of Ni-metal on timescales of 100 ps (Kachel *et al.*, 2009), and which we again observed in our experiments on capped thin Ni layers (Le Guyader *et al.*, 2023; Lojewski *et al.*, 2023). These laser-induced heating effects are a result of sample design, where the measurement geometry requires thin films on freestanding X-ray transparent substrates. Thus, the available volume allowing for heat dissipation is too small, so the heat load introduced by the laser pulse can not dissipate quickly enough. With the bunch-train X-ray delivery scheme of the European XFEL, we could analyze the pump-induced changes as a function of the accumulated number of laser pulses per train (Le Guyader *et al.*, 2023), which is shown on the right of figure 1 panel (a-c). We found that the induced changes increase

linearly with the number of laser pulses, shown in panel (c) of figure 1, as each laser pulse leads to a small local increase in the sample temperature.

However, laser-induced heating is not the only long-lived effect that can occur. It has been observed that the electron trapping mechanism can influence the dynamics on long-time scales as well. For example, Foglia *et al.* showed that defect-mediated exciton trapping can lead to excitations which persist on a ns time scale in oxides (Foglia *et al.*, 2019). Furthermore, Santomauro *et al.* showed with transient X-ray absorption spectroscopy long-lived excitations in inorganic perovskites following an optical excitation that persists up to hundreds of ns and which they link to the formation of polarons (Santomauro *et al.*, 2016). In our NiO measurements, we also find a contribution of some long-lived excitation, which appears distinctly different from the one in Ni. Instead of a linear dependence of the pump-induced change on the accumulated number of laser pulses we find in some part a saturation-like behaviour. Charge carrier trapping through polaron formation might be a possible origin of these distinctly different long-lived effects that can be observed in NiO, especially as polaron trapping has been previously observed in NiO (Biswas *et al.*, 2018), and it was shown that polaron trapping can lead to extremely long-lived excited states (Santomauro *et al.*, 2016). In this work, we disentangle the contributions of the long-lived excitations from the initial pump-induced change and analyze them in regard to time delay-, fluence dependence and their modification of the spectral shape.

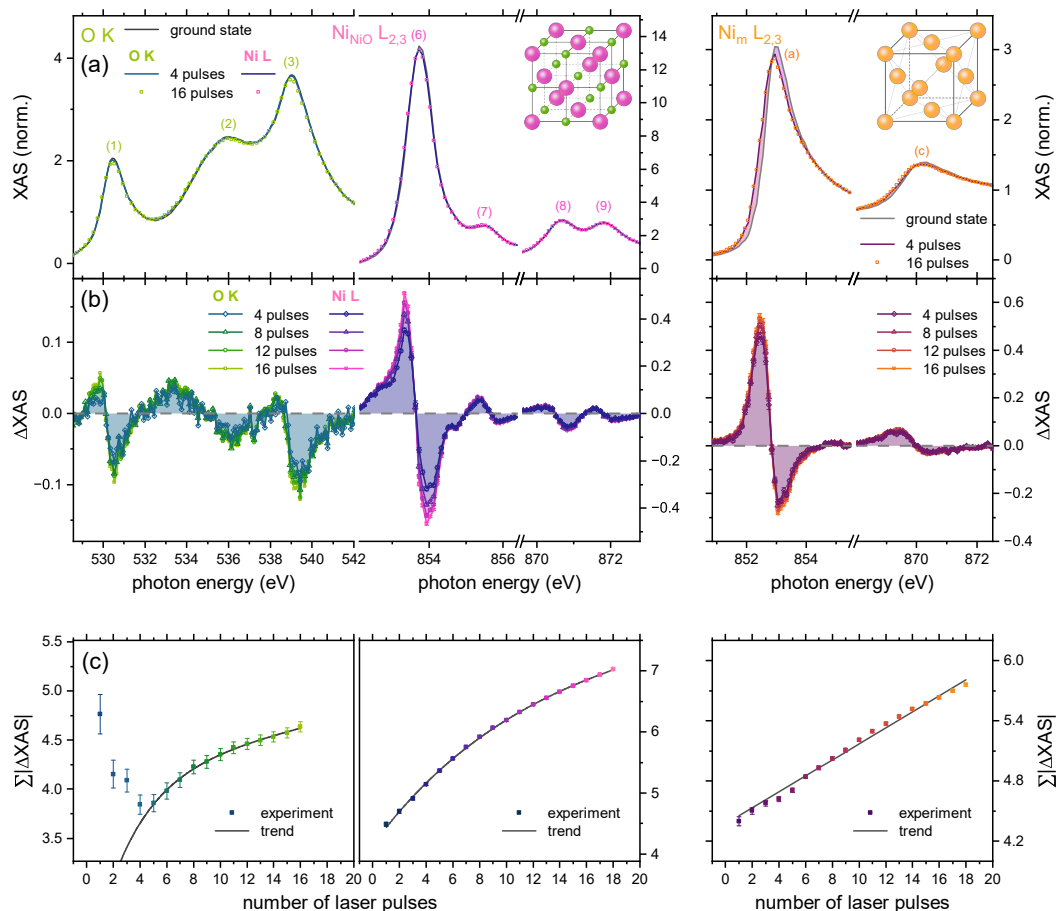


Fig. 1. (a) Exemplary X-ray absorption spectra for the NiO O K-edge (left), NiO L<sub>2,3</sub>-edges (middle) and Ni-metal L<sub>2,3</sub>-edges (right). The grey line shows the ground state absorption spectrum while the coloured line shows the excited state spectrum after 0.5 ps for NiO and 0.4 ps for Ni, after 4 accumulated laser pulses per train. The coloured dots show the excited state spectrum for the same delay using 16 accumulated laser pulses. (b) Resulting pump-induced change going from 4 to 16 accumulated laser pulses per train for the three absorption edges. (c) Absolute area encompassed by the pump-induced change as a function of an increasing number of accumulated laser pulses. The lines are a guide to the eye.

## 2. Experimental detail

### 2.1. Sample preparation

The Ni-metal and NiO samples were grown using molecular beam epitaxy (MBE) on 200 nm thick  $\text{Si}_3\text{N}_4$  membranes in a 5 x 5 and 12 x 12 grid formation for Ni and NiO, respectively. For both samples, a 100 nm thick Copper layer was deposited on the back of the substrates to be used as a heatsink and to increase stability. During the growth, some rows were masked so that the resulting bare  $\text{Si}_3\text{N}_4$  membranes can be used in combination with the beam-splitting off-axis zone plate setup (Le Guyader *et al.*, 2023) to obtain a reference signal. In the case of the Ni samples, a  $20 \pm 0.7$  nm thick fcc Ni layer was deposited on the uncovered membranes, which was later capped using a 2 nm MgO layer to avoid oxidation. For the NiO samples, a  $37.4 \pm 0.1$  nm thick NiO layer was grown by Ni evaporation under an oxygen atmosphere of  $1 \cdot 10^{-6}$  mbar. The samples were characterized using XRD and vibrating sample magnetometry to guarantee the structural and magnetic properties of the Ni and NiO samples (Lojewski *et al.*, 2023; Lojewski *et al.*, 2024). For additional details on the sample preparation, see the supplementary material of (Lojewski *et al.*, 2023; Lojewski *et al.*, 2024).

### 2.2. Experimental setup

All experimental XAS data was measured at room temperature in a stroboscopic pump-probe experiment at the Spectroscopy and Coherent Scattering Instrument (SCS) of the European XFEL (Tschentscher *et al.*, 2017; Le Guyader *et al.*, 2023; Lojewski *et al.*, 2023).

The Ni-metal samples are excited using an ultrashort (35 fs) optical laser pulse (Pergament *et al.*, 2016) with a photon energy of  $h\nu = 1.5$  eV (800 nm) and an incidence fluence of  $12$  mJ/cm<sup>2</sup>. The laser pulse causes excitations of the 3d electrons into unoccupied 4sp states that subsequently scatter and relax to an elevated



electronic temperature. The NiO samples are resonantly excited above the optical bandgap using a photon energy of  $h\nu = 4.7$  eV (266 nm) with an incidence fluence of 0.8 or 4.0 mJ/cm<sup>2</sup> to excite electrons from the O  $2p$  states into unoccupied states of the upper Hubbard band (Gillmeister *et al.*, 2020). The pump pulses are synchronized with X-ray pulses to probe the modification following the laser excitation after a time delay of  $\Delta t$ . We measure the Ni  $L_{2,3}$ -edges for both Ni-metal and NiO using monochromatic (Gerasimova *et al.*, 2022) linearly polarised X-ray with energies tuned between 840 and 880 eV to excite  $2p_{3/2}$  or  $2p_{1/2}$  core electrons into unoccupied  $3d$  final states. In addition, for NiO, the O K-edge is also measured using X-ray energies between 525 and 565 eV to excite  $1s$  core electrons into unoccupied  $2p$  states.

All measurements were performed with the beam-splitting off-axis zone plate (BOZ) setup (Döring *et al.*, 2020; Le Guyader *et al.*, 2023) of the SCS instrument. The zone plate focuses and splits the incoming X-rays into three distinct beams according to the  $0^{th}$ ,  $-1^{st}$  and  $1^{st}$  diffraction order, which allows the measurement of three spatially separated regions simultaneously. For transient pump-probe XAS measurements, this setup is used to measure the ground-, excited- state and reference signal concurrently. All measurements were performed in transmission geometry by detecting the X-ray intensity following transmission through the sample with a fast 1 Mpixel X-ray imager (DSSC camera) (Porro *et al.*, 2021). The X-ray delivery for the experiments followed the bunch-train scheme (Tschentscher *et al.*, 2017; Le Guyader *et al.*, 2023). So, the X-ray absorption spectra were measured using bursts (trains) of high repetition rate X-ray pulses with an intra-train repetition rate of 70 kHz (14.3  $\mu$ s) or 57.5 kHz (17.4  $\mu$ s) for Ni or NiO, respectively. The burst (trains) are delivered with a train repetition rate of 10 Hz. The bunch-train delivery pattern was adjusted between experiments so that for the Ni metal measurements, a total of 25 pump-probe synchronized pulses were used, which was reduced to 18 synchronized pulses when measuring the NiO Ni

L-edges with a pump fluence of  $4 \text{ mJ/cm}^2$ . The pattern was further changed for the measurements of the oxygen K-edge and the NiO Ni L-edges with a pump fluence of  $0.8 \text{ mJ/cm}^2$  by dropping the first and last X-ray pulse, leaving only 16 pump-probe synchronized pulses. In this analysis, we only use the first 18 pulses from the Ni-metal measurements, but we have previously shown with another dataset that the linearly increasing behaviour with the number of laser pulses, as highlighted by figure 1 c), remains the same even for more accumulated laser pulses (Le Guyader *et al.*, 2023).

The XAS data is initially processed and evaluated with the dedicated SCS toolbox (Le Guyader *et al.*, 2023; Fangohr *et al.*, 2020; SCS-team, 2024) by calculating the negative logarithm of the transmitted ground- or excited-state signal, divided by the reference signal. Additionally, the flat field and non-linearity correction detailed in (Le Guyader *et al.*, 2023) are applied. The toolbox also allows for a separation of the data according to the accumulated number of laser pulses within each train, which we use to characterize the secondary long-lived effects. Following this initial processing, the XAS data is exported for each spectrum and optical laser pulse for further evaluation, which is described in the following section. The raw data of all experiments shown in this publication is publicly available. For details, see section 7 or (Lojewski *et al.*, 2020; Lojewski *et al.*, 2021).

### 3. Data processing

As we aim to disentangle and discuss the primary contribution from the pump-induced changes and the secondary contribution building up through long-lived excited states, we have to ensure comparability between the XAS spectra, especially with changes in the experimental setup between experiments. To that end, we perform a background correction and normalize the spectra to the invariant edge jump (Wang *et al.*, 2018), as we will detail in the following section. Additionally, we can apply the modelling

approach that we previously used to great success in modelling the induced change itself (Lojewski *et al.*, 2023; Lojewski *et al.*, 2024) to also model the secondary contribution of long-lived effects.

### 3.1. Background correction and normalization

One exemplary NiO Ni L<sub>2,3</sub> - absorption spectrum ( $\Delta t = 0.5$  ps), as obtained from the toolbox evaluation, is shown in panel (a) of figure 2 on the left with the corresponding pump-induced change ( $\Delta XAS$ ) on the right. Between the ground and excited state spectra, a clear offset is visible, which we attribute to some minor differences in the -1<sup>st</sup> and 1<sup>st</sup> order beams split by the zone plate. This difference is also visible in the  $\Delta XAS$  as an offset. In addition, the spectra diverge slightly with increasing X-ray energy, which could also be linked to the zone plate setup. Both of these effects are corrected using a background correction. For the background correction, we take two regions where no pump-induced changes are visible, which are the L<sub>3</sub> pre-edge (848.2 - 851.2 eV) and L<sub>2</sub> post-edge region (875.2 - 878.2 eV), highlighted by the green shading in figure 2. As there is a slightly increasing slope in these regions, we fit two linear functions, shown as dashed grey lines in figure 2, to obtain a mean value for the beginning and end of each region, respectively, which is displayed as orange data points. Using these four mean values, we can construct the linear background shown in figure 2 as the green line. The  $\Delta XAS$  is then corrected by subtracting the background, while the spectra are corrected by subtracting two linear functions with half the slope and opposite signs pulling them on top of one another. The results of this background correction are shown in panel (b) of figure 2. Following the correction, the ground and excited state spectra coincide perfectly in the pre and post-edge region, and the  $\Delta XAS$  also shows zero induced changes in these regions. The spectra are then normalized so that the mean L<sub>3</sub> pre-edge region, highlighted by the blue shading in

panel (b) of figure 2, corresponds to zero, while the  $L_2$  post-edge region, which corresponds to the invariant edge jump and is marked by the red shading, corresponds to one. The  $\Delta XAS$  is normalized accordingly, and the final results are shown in panel (c) of figure 2.

The background correction and normalization of the Ni metal Ni  $L_{2,3}$  - absorption edge is done in exactly the same way and is, as such, not further shown.

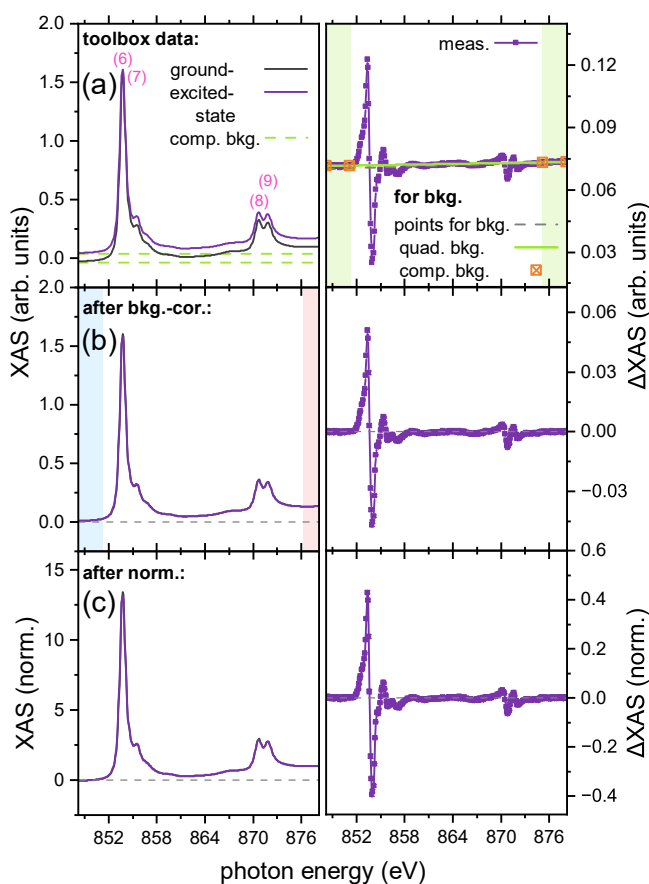


Fig. 2. (a) Exemplary background correction of a NiO  $L_{2,3}$  ground and excited state spectrum [ $\Delta t = 0.5$  ps] (left), as well as the pump-induced change (right). The linear background (green solid line) is constructed from four points (orange squared) describing the average value at the beginning and end of the pre- and post-edge region (right). (b) The absorption spectra are normalized so that the pre-edge (blue area) corresponds to zero and the post-edge (red area) corresponds to one. (c) Final normalized spectra (left) and corresponding pump-induced change (right).

For the oxygen K-edge, the ground and excited state spectra also show a slight offset like the Ni L<sub>2,3</sub> - edge, but in addition, they no longer diverge linearly with the X-ray energy but rather show a quadratic dependence, as highlighted in figure 3 a) with the grey dashed line. As such, the linear approximation of the background is no longer possible, and a quadratic function has to be used instead. In order to obtain a good approximation of the background with the quadratic function, we choose, in addition to the pre- (525-528 eV) and post-edge regions (563 - 564.8 eV), an additional region between the fourth and fifth fine-structure peak (547.5 - 550 eV). From our modelling, as described later in this section, we expect this region to show no induced changes that would be the result of an energy shift or broadening. The three regions used as reference for the background correction are marked with green shading in panel (a) of Figure 3. Instead of determining two mean values per region as done before with the Ni L - edges, we find better results by using all data points in this region directly to fit the quadratic function. The data points used for the background correction are also highlighted in orange in panel (a) of Figure 3. The resulting quadratic background is shown in panel (a) of Figure 3 as a grey dashed line. In addition we find another modification that occurs even for a static measurement. This modification is visible in the first X-ray pulse of the train even before the first laser excitation and appears between the first and fourth fine-structure peaks. This contribution is apparent immediately in the first measurement at that sample position and remains unchanged for all measurements. So, after subtracting the previously determined quadratic background for each scan, we average the  $\Delta$ XAS to obtain a better description of the remaining modifications. The average is shown in the top part of panel (b) in figure 3. To further differentiate the contributions from the noise, we investigate the distribution of data points in the pre- and post-edge regions (orange data points) and the region of interest between the first and fourth fine structure peaks (blue data points), which is shown to

the left of panel (b). The distribution of data points in the pre- and post-edge regions shows a normal distribution, indicating that these regions include only noise and no distinguishable features. The distribution in the region of interest, however, deviates strongly from a normal distribution and appears much broader compared to the pre- and post-edge regions. To clearly separate the contributions from random noise spikes, we use the 95-5 percentile of the pre- and post-edge distribution, with any modification where three or more connected data points that lie outside of this region should be considered to be real contributions. This region is shown in panel (b) of figure 3 as the dotted orange lines. Using this selection criterium, we can identify one narrower positive modification around 529.7 eV, followed by a broader negative modification between 534.5 and 543 eV. To describe these modifications, we use a multiple-curve fit with up to four Lorentz curves, which are fitted simultaneously. From the fit, we obtain a description of the modifications with three Lorentz curves, which are shown in figure 3 as the dashed, dotted and dashed-dotted lines. The combination of these three contributions makes up the additional background correction, which is shown in the figure as a straight line. Using this correction, we can fully correct the modifications as shown at the bottom in panel (b) of figure 3. Following the correction, the distribution of data points exactly matches the distribution that results from the noise.

At this point, we want to stress that these modifications are distinctly different from the other modifications discussed in this work and also from laser-induced sample damage, which we could observe at a different window in one scan (see appendix of (Lojewski *et al.*, 2024) for more details). We attribute this difference to non-completely homogeneous sample properties across the three membranes used for the measurement, which could be the result of technical limitations with our MBE chamber. For one, the evaporation cells are slightly offset in regards to the sample normal and, as such,

evaporate at an angle. This can lead to thickness variations of up to 2 % over the area of the three membranes. Additionally, in our chamber, it is not possible to grow samples at high temperatures and in an oxygen atmosphere. As a result, the NiO samples were grown at room temperature, which could cause low vacancy mobility and could result in a nonuniform distribution of oxygen vacancies between the membranes.

Nevertheless, this effect can be corrected using this additional background correction, which is also implemented for the rest of the oxygen K-edge spectra, resulting in the pink solid line in panel (a) of figure 3. Similar to the Ni L-edges, we correct both the ground and excited state spectra by pulling them on top of one another and subtracting the complete background from the pump-induced change. The results of this complete background correction are shown in panel (c) of figure 3. Afterwards, the spectra are normalized as was done before with the Ni L-edge spectra by setting the mean value in the pre-edge region (highlighted by blue shading) to zero and the mean value in the post-edge region (highlighted by red shading) to one. For the oxygen K-edge, we choose the post-edge region just behind the fourth fine-structure peak, as the region behind the sixth fine-structure peak is not sufficient for comparable normalization. The results of the normalization are shown in panel (d) of figure 3.

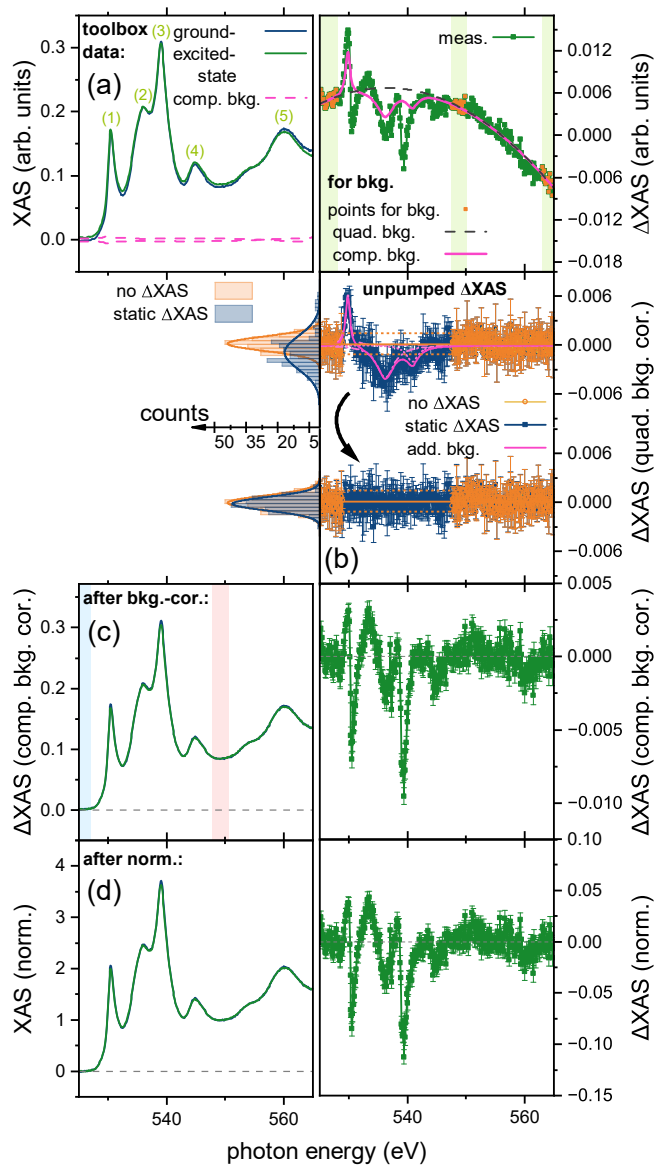


Fig. 3. (a) Exemplary background correction of a NiO oxygen K-edge ground and excited state spectra [ $\Delta T = 0.5$  ps] (left), as well as the pump-induced change (right). A quadratic background (dashed grey line) is constructed by fitting the  $\Delta XAS$  in the green highlighted regions (orange squared). (b) Additional background contribution that results from a static difference between the two membranes, which is corrected using the total background (pink solid line). (c) The absorption spectra are normalized so that the pre-edge (blue area) corresponds to zero and the post-edge (red area) corresponds to one. (d) Final normalized spectra (left) and corresponding pump-induced change (right)



### 3.2. Modelling the Pump-induced Change

An important part of analyzing the observed pump-induced changes is disentangling the underlying modifications of the spectrum that cause them. To accomplish this, we model two of the most common modifications observed in transient X-ray absorption spectroscopy, namely a rigid energy shift (Stamm *et al.*, 2007) and a spectral broadening (Carva *et al.*, 2009), and fit the results to the experimental data. This not only helps us identify the individual contributions of this energy shift and broadening but also additional modifications that cannot be described by the modelling.

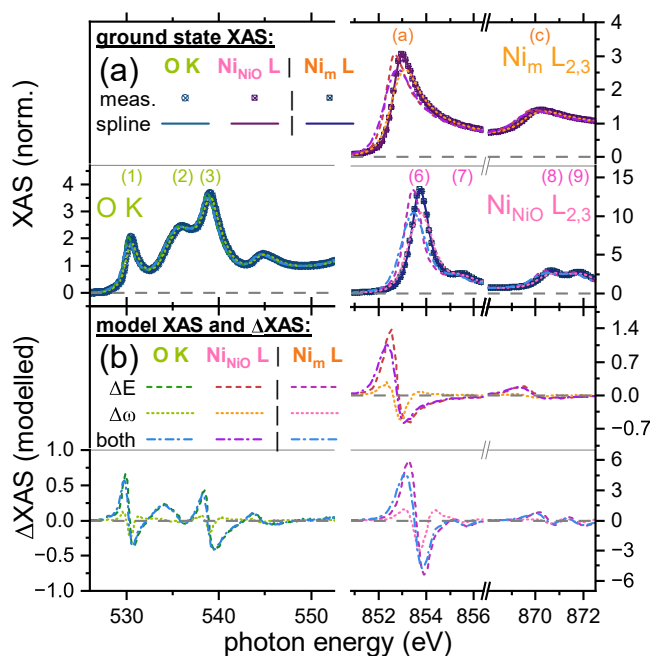


Fig. 4. (a) Ground state spectra of the Ni-metal Ni  $L_{2,3}$ -edge (top), NiO Ni  $L_{2,3}$ -edge and oxygen K-edge (bottom) with modelled curves for no modification (solid), energy shift only (dashed line), broadening only (dotted line) and a combination of the two (dashed-dotted line) with resulting  $\Delta XAS$  in (b).

To model the  $\Delta XAS$ , we start by calculating an Akima spline of the ground state spectrum, which allows us to freely shift the energy during the modelling by shifting the axis of the spline by the amount  $\Delta E$  relative to the unpumped spectrum. The

broadening is modelled by convoluting the spline with a Gaussian with the full-width half maximum (FWHM)  $\omega$ . Exemplary modelled curves for each absorption edge are shown in figure 4 (a) for an energy shift only, a broadening only and a combination of the two.

The resulting pump-induced change of these modifications is then calculated as the difference between the original ground state spectrum and the modified Akima spline. The  $\Delta$ XAS for each modelled curve is shown in panel (b) of figure 4. In order to describe the experiments, the modelled changes are then compared to the pump-induced changes, and the two parameters  $\Delta E$  and  $\omega$  are adjusted to minimize the difference between the two. For the result presented here, we use the ground state spectrum with the maximum number of X-ray pulses as it offers the best data quality and does not change with the number of pulses. Furthermore, to characterize the influence of the long-lived effects, we fit a selection of curves simultaneously, which allows us to keep one parameter fixed for curves with a different number of laser pulses and optimize it globally instead. This approach offers the advantage that it is possible to try and model the effect of the long-lived states by variation of only one of the parameters, which is of great interest in disentangling the origin of these effects.

## 4. Results

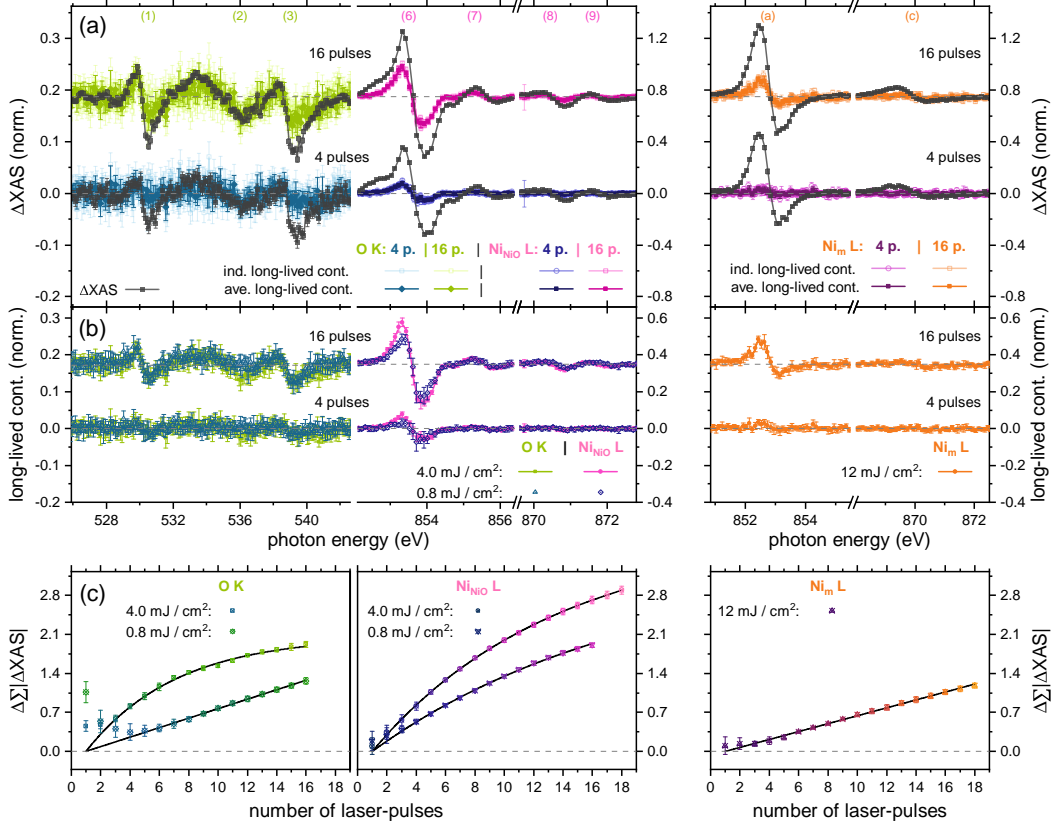


Fig. 5. (a)  $\Delta XAS$  for each absorption edge after 4 and 16 accumulated laser-pulses compared to the individual contribution of long-lived effects with the average contribution overlaid. (b) Average contribution of long-lived effects after 4 and 16 accumulated laser-pulses for 0.8 and 4.0  $mJ/cm^2$ . (c) Average change in the absolute area encompassed by the pump-induced change as a function of an increasing number of accumulated laser pulses.

In this work, we aim to separate the contribution of secondary long-lived excitations from the initial pump-induced excitations. In order to do that, we divide each measurement into sub-scans according to the number of accumulated laser pulses per train. As a result, we obtain either sixteen or eighteen ground-, excited state spectra with the corresponding  $\Delta XAS$ . To disentangle the individual contributions in the  $\Delta XAS$ , we subtract the signal measured after just the first laser pulse in each train,

representing purely the initial pump-induced change, from subsequent scans, which include multiple laser excitations. Doing this allows us to investigate how the shape of the secondary contribution changes after a certain number of laser excitations per train (figure 5 (a-b)) and how the area under the  $\Delta$ XAS evolves with the number of laser pulses (figure 5 (c)) for different time delays  $\Delta t$  and incidence fluence.

Figure 5 panel (a) shows the individual contributions of the long-lived excitations measured at different time delays  $\Delta t$  as semi-transparent lines in the background in comparison with an exemplary pump-induced change measured after a time delay  $\Delta t$  of 0.5 ps for NiO and 0.4 ps for Ni-metal. All the individual contributions show the same shape and scale of modification for all absorption edges after both four and sixteen laser excitations. This indicates that the rise time of these secondary longer-lived excitations is much longer than the initial time delay  $\Delta t$  of the experiment, so their contribution during the first initial laser excitations is comparably small for all measurements. To allow for a more rigorous discussion of changes in shape and scale of these long-lived contributions for different numbers of accumulated laser pulses and the two incidence fluence, the individual contributions are averaged, which is shown as the solid overlaid curve in Figure 5 panel (a).

Figure 5 panel (b) shows the average contribution of the long-lived excitations after four and sixteen accumulated laser excitations per train and for a pump incidence fluence of 0.8 and 4.0 mJ/cm<sup>2</sup> for NiO and 12 mJ/cm<sup>2</sup> for Ni-metal. In general, the shape of these contributions appears to follow the shape of the  $\Delta$ XAS itself, with only some minor differences. At the NiO Ni L-edge, the pre-edge feature around 852.6 eV, which we discuss more extensively in (Lojewski *et al.*, 2024), is entirely unaffected by long-lived effects. Additionally, the NiO L<sub>3</sub>-satellite (7) shows some differences compared to  $\Delta$ XAS. At the NiO O K-edge, the long-lived effects show a more symmetrical modification, with the differences being most apparent around the

1st and 3rd fine structure peaks (1,3). The Ni-metal L-edges show no major differences between the long-lived contribution and the  $\Delta$ XAS other than the intensity. Figure 5 (b) also shows how the shape of the long-lived excitations evolves with the accumulated number of laser excitations per train. For all the absorption edges, the contribution of the long-lived excitations increased with an increasing number of pulses, resulting in the increase of the absolute area previously shown in figure 1 panel (c). The number of pulses per train generally does not appear to influence the shape of the induced change but only increases the intensity. The incident fluence of the pump pulse does, however, affect both the shape and intensity of the induced changes, which can be seen directly at the NiO L<sub>3</sub>-edge. At the NiO L<sub>3</sub>-edge, the excitation with 4.0 mJ/cm<sup>2</sup> results in a stronger positive change around 853.3 eV, while the negative change at 853.9 eV is fairly similar for both 0.8 or 4.0 mJ/cm<sup>2</sup>. This difference becomes more accentuated with an increasing number of laser pulses per train, as seen in figure 5 (b). In contrast, the O K-edge does not display as strong a dependence on the pump fluence as the NiO L-edges, with the contribution of the long-lived excitations showing mostly the same shape for the two pump fluences. The only difference appears after sixteen laser pulses around the 2nd fine structure peak (2).

Figure 5 panel (c) shows the average increase in the absolute area of the long-lived excitations. The increase of the absolute area also appears to be independent of the initial time delay  $\Delta t$ , showing the same trend for each absorption edge and fluence, which, as discussed before, further indicates that the contribution of these long-lived excitations is rather small on the initial timescales. However, if the noise level is high with respect to the long-lived contribution, the level of noise itself contributes significantly to the sum and causes a difference between measurements. This results in a larger error and elevated values for the first laser pulses as random noise fluctuations are the majority contributor to the sum, which can be seen at the O K-edge for

0.8 mJ/cm<sup>2</sup>.

As before, an increase in the absolute area due to the contribution of the long-lived excitations appears independent of the time delay of individual measurements so that the average of multiple measurements can be used. The only difference between measurements can be observed for the first few laser pulses where the noise level is large. Here, the contribution of summing over the noise can outweigh the contribution of the secondary effects, leading to an initially larger absolute area, which first decreases before increasing with the number of laser pulses, as seen for the O K-edge. Comparing the increasing trend for the two laser fluences further accentuates the fast increase of the long-lived contributions at the larger pump fluence. Additionally, comparing the behaviour of the contributions in the Ni-metal and NiO samples further highlights the different trends for the two samples, with a linear increase in Ni-metal and a more saturating type of behaviour in NiO. We emphasize this difference by describing the trend with the following function:

$$\Delta \sum |\Delta XAS|(n) = A_1 \cdot \left(1 - \exp\left(\frac{-(n-n_0)}{\theta}\right)\right) + A_2 \cdot (n - n_0),$$

Here, the first term describes a saturating behaviour while the second term describes the linear behaviour, with  $n$  as the number of accumulated laser pulses per train,  $n_0$  as the first pulse and  $A_{1,2}$  corresponding to the amplitude of the individual terms. The description using this function aims to separate the linear contribution, which is most likely related to a local increase in temperature from the saturating behaviour, which could be linked to other effects like polaron formation, as a saturation effect for polaron formation as a function of laser fluence has been previously observed (Zhang *et al.*, 2023). For the Ni-metal L-edges, the fit clearly shows a linear dependence with a slope of  $0.071 \pm 0.001$ . For the NiO L<sub>3</sub> edge, the fit shows predominantly a saturating behaviour with a similar amplitude  $A_1$  of  $3.4 \pm 0.1$  and  $3.55 \pm 0.68$  for 0.8 and 4.0 mJ/cm<sup>2</sup>, respectively, with the number of pulses necessary to reach saturation

$\theta$  decreasing from  $17.83 \pm 0.65$  to  $11.71 \pm 1.53$ . A small linear contribution might be present for  $4 \text{ mJ/cm}^2$ , which shows a linear slope  $A_2$  of  $0.01 \pm 0.02$ . However, due to the error, a clear separation between linear and saturating contributions can not be made. For  $0.8 \text{ mJ/cm}^2$  the slope of the linear contribution becomes deminishingly small. The O K-edge excited with  $4.0 \text{ mJ/cm}^2$  shows a saturating behaviour with an amplitude  $A_1$  of  $2.07 \pm 0.04$  and the number of pulses necessary to reach saturation  $\theta$  being  $6.16 \pm 0.27$ , while the slope of the linear contribution goes towards zero. The excitation with  $0.8 \text{ mJ/cm}^2$  shows a mostly linear response with a slope of  $0.085 \pm 0.001$ . However, because the noise level is so high at the oxygen K-edge compared to the relatively small contribution of both the pump-induced change and the contribution of long-lived excitations, it becomes difficult to make a conclusive statement regarding the evolution of the long-lived excitations.

Overall this analysis highlights the challenge with these accumulative effects. As the contribution of these long-lived effects increases with the number of laser pulses, the overall pump-induced change becomes increasingly dominated by these long-lived contributions as more laser pulses per train are included. Hence, one approach to limiting these effects is to reduce the number of laser pulses per train, which comes at the detriment of data quality or measurement time. We have previously shown that by limiting the number of laser pulses we use for the data analysis and additionally compensating for the evaluation of uncertainty while modelling, we can deal successfully with these modifications (Lojewski *et al.*, 2023; Lojewski *et al.*, 2024). In this paper, we want to present a different approach where we aim to separate and analyze the contribution of these long-lasting effects individually from the pump-induced modifications, as well as attempt to correct the  $\Delta\text{XAS}$  measured with a higher number of pulses. To that end, we applied our modelling approach to further evaluate their shape.

## 4.1. Modelling

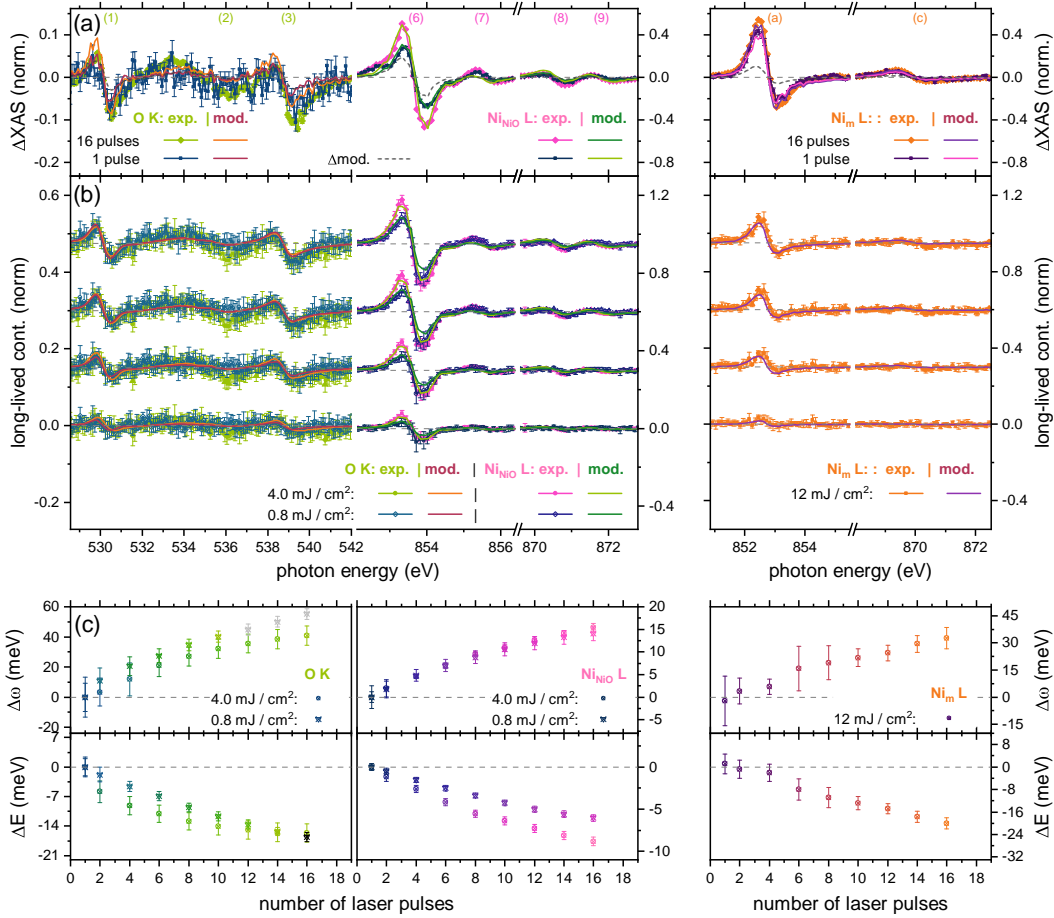


Fig. 6. (a) Modelling of  $\Delta XAS$  for 1 and 16 laser pulses of the O K, NiO L and Ni L-edges, with the corresponding modelled heating contribution shown as a dashed line. (b) Comparison of average measured and modelled heating contribution after 4,8,12 and 16 for all pump fluences. (c) Modelling parameter for the energy shift  $\Delta E$  and broadening  $\Delta\omega$  for the two fluences as a function of accumulated laser pulses.

We model the contribution of the long-lived effects by modelling the  $\Delta XAS$  after multiple laser pulses per train and comparing how the modelled changes compared to the modelled  $\Delta XAS$  after one laser pulse. To that end, we model, as earlier described, the  $\Delta XAS$  after one, two and every subsequent two laser pulses simultaneously. As the



groundstate spectrum remains unmodified regardless of the number of X-ray pulses per train except for the level of noise, we use the spectrum measured with the maximum number of X-ray pulses as a basis to model all  $\Delta$ XAS signals in order to obtain the best modelling quality. Modelling all curves simultaneously allows us to also set one parameter, either the energy shift  $\Delta E$  or broadening  $\Delta\omega$  to be optimized globally for all  $\Delta$ XAS signals, using only the remaining free parameter to model the contribution of the long-lived excitations. However, overall, we found that to obtain the best result, both parameters should be varied to describe the contribution of the long-lived excitations for all measurements across all absorption edges. We obtain the contribution of the long-lived excitations as before by calculating the difference between the modelled  $\Delta$ XAS after multiple laser pulses per train and the modelled first initial laser excitation. This approach is shown exemplarily in figure 6 panel (a) for a measurement with a time delay  $\Delta t$  of 0.5 ps for the NiO absorption edges and 0.4 ps for the Ni-metal L-edges. We average the different modelled contributions to obtain an average modelled contribution of the long-lived excitations, which is shown in comparison with the average measured contribution in figure 6 panel (b).

Overall, the modelling manages to capture the shape of the contribution fairly well for all absorption edges, with only some minor deviations. At the oxygen K-edge, the modifications of the second fine structure peak (2) are not captured well for a higher number of excitations per train. The contribution of long-lived excitations around the first and third fine structure peaks (1,3) seems mostly well described, although the modelling itself does not work too well in these regions for the  $\Delta$ XAS. For the NiO  $L_3$ -edge, the model works extremely well in describing both the overall  $\Delta$ XAS as well as the contribution of long-lived excitations. The only deviations that are visible are at the pre-edge feature, which results from non-equilibrium multiple excitations, is unaffected by the long-lived effects and also not captured by the modelling (Lojewski

*et al.*, 2024), as well as the  $L_3$  satellite (7) where both the modelling of the  $\Delta XAS$  and the long-lived contributions fails. Additionally, there are also differences visible in both the modelling of the  $\Delta XAS$  and the long-lived contributions at the first peak of the NiO  $L_2$ -edge (8). At the Ni-metal L-edges, the modelling also works fairly well, accurately capturing the shape of both the overall  $\Delta XAS$  as well as the contribution of the long-lived excitations, with the only deviation being visible at the reversal point between the positive and negative induced change (852.8 eV). Panel (c) of figure 6 shows the change of the determined energy shift  $\Delta E$  and broadening  $\Delta\omega$  for increasing the number of laser pulses per train.

For the Ni metal L-edges, we find that both the energy shift and broadening increase linearly, with the number of laser pulses per train. At the NiO L-edges, the shift and broadening both seem to saturate. However, while the energy shift shows a strong fluence dependence, we find no influence of the fluence on the determined broadening. This difference in the energy shift can be directly observed in the shape of the long-lived contribution as the positive contribution around 853.3 eV increases faster with the number of pulses per train, while the negative contribution at 853.8 eV stays mostly the same.

For the O K-edge the energy and broadening also show a saturating type behaviour. However, we find the behaviour of the fluence dependence to be directly contradictory to the changes in the absolute area observed earlier. We find that the value of the broadening seems to increase faster with the lower pump fluence. The determined energy shift, although initially increasing faster, also seems to saturate earlier, while the energy shift for 0.8 mJ/cm<sup>2</sup> continues to increase further. This contradiction is most likely a combination of the higher noise level at the O K-edge and the overall model not completely accurately describing the  $\Delta XAS$ . We previously emphasized the modification around the second fine-structure peak (2) as the most prominent

difference between 0.8 and 4.0 mJ/cm<sup>2</sup>, which is incidentally not accurately captured by the modelling. From this, we conclude that the modelling approach is not well suited to describe the differences between the two pump fluences at the O K-edge.

## 5. Discussion

We have previously discussed the effects of long-lived excitations in Ni-metal as a local heat increase (Le Guyader *et al.*, 2023). The local heating is the consequence of the sample geometry needed for the employed setup, requiring the Ni-layer to be sandwiched between an X-ray transparent but also weakly heat-conducting substrate and the insulating capping layer to prevent oxidation. Thus, the heat transport out of plane is severely limited, and heat transport can only occur in-plane. As a result, the energy is not completely dissipated between the laser pulses during a train, so the heat of the pumped spot continuously increases within a train. We have now extracted the secondary modification that results from this local heat increase and found that it mirrors the shape of the initial induced changes but with reduced intensity. Exactly this behaviour has been previously observed by T. Kachel *et al.* in Ni-metal for laser-induced heating after 100 ps, where they identified an energy shift of 38 meV (Kachel *et al.*, 2009). We find comparable values of the energy shift, which reaches  $20 \pm 2$  meV after 16 laser pulses. This further cements this modification as a local increase in the temperature, as we previously outlined (Le Guyader *et al.*, 2023).

For NiO, the contribution of the long-lived excitations increases non-linearly, which we would not expect for a purely local heating-induced effect. For metal oxides, it was previously shown that charge carrier trapping through exciton (Foglia *et al.*, 2019) and polaron (Biswas *et al.*, 2018; Carneiro *et al.*, 2017) formation causes long-lived excitations. These excitations have been shown to be extremely long-lived, existing for hundreds of ns (Foglia *et al.*, 2019; Santomauro *et al.*, 2016), making them a potential

reason for different behaviour observed in NiO. Theoretical calculations show that for NiO, small polaron formation is possible by trapping a photoexcited electron on a Ni-site through an extension of the surrounding oxygen atoms (Yu *et al.*, 2012). The formation of polarons in NiO has been previously observed by S. Biswas *et al.* (Biswas *et al.*, 2018) in XUV spectroscopy of the Ni M<sub>2,3</sub>-edge as a reduction of photo-induced redshift, with the reduced redshift persisting over tens of ps. This could link the occurrence of the long-lived energy shift that we observe at the Ni L-edges of NiO to the formation of polarons. Additionally, in black  $\gamma$ -CsPbI<sub>3</sub> it was demonstrated that the formation of polarons not only scales with the laser fluence but also reaches a stable regime where the polaron formation saturates (Zhang *et al.*, 2023). This could further explain the saturating behaviour of the energy shift that we observe at the NiO Ni L-edges. In addition, the formation of polarons could also be related to the long-lived modification that we observe at the O K-edge. As the polarons are stabilized through an extension of the oxygen atoms surrounding the Ni site, this should influence the Oxygen K-edge spectrum, especially as it was shown that it is sensitive to lattice excitations in MgO (Rothenbach *et al.*, 2019; Rothenbach *et al.*, 2021).

## 5.1. Correction Methodes

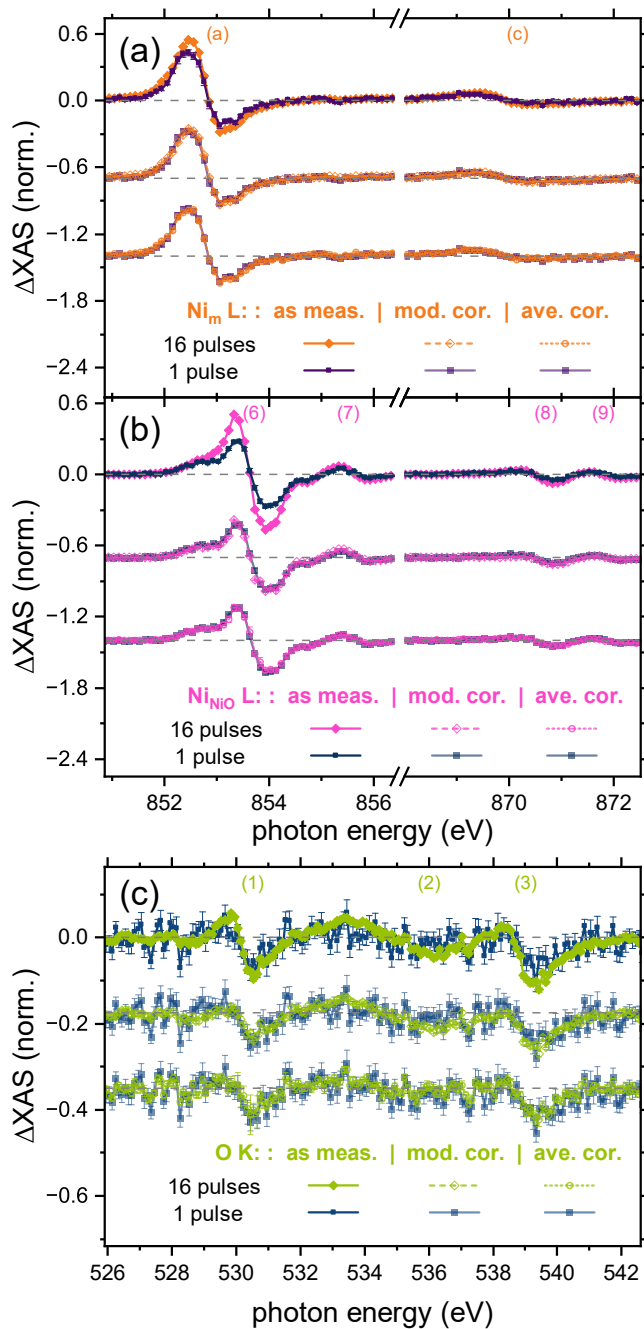


Fig. 7. Comparing the  $\Delta XAS$  after one and sixteen accumulated laser pulses as measured, using the modelled long-lived contribution for correction and using the average long-lived contribution for correction for the Ni-metal L-edges (a), NiO L-edges (b) and O K-edge (c).

We have previously discussed that the effects of these long-lived excitations can be minimized by limiting the number of laser pulses per train, and while this is a valid approach, it might not always be the best option. If the pump-induced change is relatively small compared to the noise level, it might not be possible to limit the number of pulses per train too much, and this, in combination with the non-linear behaviour observed in NiO, can lead to a significant contribution in the  $\Delta$ XAS. With our analysis, we could separate the contribution of the long-lived excitations from the initial laser-induced excitations and describe their main underlying modifications using our modelling approach. Now, we want to apply these results to discuss two possible correction methods that could be used to disentangle the initial pump-induced changes from the long-lived effects while utilizing more pulses per train. For one, we can use our modelled contribution of the long-lived excitations to correct the measured  $\Delta$ XAS. Alternatively, the average heating contribution can also be used to apply a correction. Figure 7 shows a comparison between the  $\Delta$ XAS measured with one or sixteen pulses per train for the Ni-metal L-edges (a), NiO L-edges (b) and O K-edge (c) and the results of the two correction methods. In general, using the modelled contribution for the correction gives the best signal-to-noise ratio but has a big disadvantage in that it only works if the modelling completely accurately captures all long-lived modifications. This is not the case with our simplified modelling approach, which leads to some visible deviations at the NiO L<sub>3</sub> Satellite (7) and the second fine structure peak of the O K-edge (2). Alternatively, the average measured contribution can also be used to correct the  $\Delta$ XAS, which is shown at the bottom of panel (a-c). This approach gives the best result for the overall correction but shows a signal-to-noise ratio that is a bit worse than the correction using the modelled contribution. The advantage of using the average over the model is that the more scans that have been measured, the better the correction will work. In general, both these correction methods appear

to work relatively well, but overall, we would still recommend reducing the number of laser pulses per train over these correction methods if applicable or adjusting the measurement pattern to reduce the effects. However, if the contribution of the long-lived states increases rapidly with the first few laser pulses and the pump-induced change is relatively small compared to these contributions, as we showed here with the O K-edge, one of the two proposed corrections may be used.

## 6. Conclusion

We showed the effects of long-lived excitations in high-repetition rate stroboscopic transient X-ray absorption spectroscopy measurements on nickel and nickel oxide. We identified these long-lived excitations as an additional modification of the  $\Delta$ XAS that appears and increases with an increasing number of laser pulses during the short burst measurements (trains) of the European X-ray free electron laser. In the here presented analysis, we could disentangle their contribution from the initial pump-induced change and analyze them separately using our modelling approach. In Ni, the long-lived effects lead to a linearly increasing broadening and energy shift of the Ni L-edges. The linear behaviour and shape of these contributions links the effect to local laser-induced heating, which is the result of the sample geometry limiting the only efficient heat transport to be in-plane. In NiO, these effects lead to increased broadening and energy shift of the Ni L-edges, which appear to saturate for a higher number of pulses. Additionally, the O K-edge also shows an increased broadening and energy shift, which indicates a saturating behaviour. By disentangling these long-lived contributions, we found that the energy shift of the Ni L-edges is strongly affected by the excitation fluence while the broadening is mostly unaffected. Long-lived energy shifts have been previously observed in NiO and were linked to charge carrier trapping through polaron formation on a Nickel atom site, which is stabilized through an oxygen

lattice expansion. Polaron formation could also explain the strong dependence of the energy shift on the excitation fluence and the saturating behaviour of these long-lived excitations. Furthermore, the expansion of the oxygen lattice due to the polaron formation could be linked to the modification of the O K-edge. Finally, we used our evaluation and modelling of these contributions to devise two correction methods that can help extract the initial pump-induced change without limiting the number of laser pulses per train, which allows for a better signal-to-noise ratio.

## 7. Data availability

The raw data on Ni and NiO shown in this publication are publicly available. The raw data measured on the Ni samples in experiment UP2161 is available at <https://doi.org/10.22003/XFEL.EU-DATA-002161-00> (Lojewski *et al.*, 2020). The raw data measured on the NiO samples in experiment UP2589 is available at <https://doi.org/10.22003/XFEL.EU-DATA-002589-00> (Lojewski *et al.*, 2021).

### Acknowledgements

We acknowledge the European XFEL in Schenefeld, Germany, for the provision of X-ray free-electron laser beamtimes UP2161 (Lojewski *et al.*, 2020) and UP2589 (Lojewski *et al.*, 2021) at the SCS instrument and thank the staff for their assistance. We thank Prof. Dr. Peter Fischer, Dr. Charles-Henri Lambert and Dr. Jun Zhu for their support and expertise during experiment UP2161. We thank Prof. Dr. Gheorghe S. Chiuzbăian for his contribution to the experiment UP2589. Funded by the Deutsche Forschungsgemeinschaft (DFG, German Research Foundation) through Project No. 278162697 - SFB 1242. U.B. acknowledges support from the Deutsche Forschungsgemeinschaft (DFG, German Science Foundation) through FOR 5249-449872909 (Project P6). P. S. M., R. Y. E. and M. B. acknowledge funding from the Helmholtz Association



[grant number VH-NG-1105].

## References

- Ackermann, W., Asova, G., Ayvazyan, V. *et al.* (2007). *Nature Photonics*, **1**(6), 336–342.
- Allaria, E., Baboi, N., Baev, K., Beye, M., Brenner, G., Christie, F., Gerth, C., Hartl, I., Honkavaara, K., Manschwetus, B., Mueller-Dieckmann, J., Pan, R., Plönjes-Palm, E., Rasmussen, O., Rönsch-Schulenburg, J., Schaper, L., Schneidmiller, E., Schreiber, S., Tiedtke, K., Tischer, M., Toleikis, S., Treusch, R., Vogt, M., Winkelmann, L., Yurkov, M. & Zemella, J. (2021). In *Proceedings of the 12th International Particle Accelerator Conference, IPAC2021, Campinas, SP, Brazil*, p. 4. JACoW Publishing, Geneva, Switzerland. Backup Publisher: 12th International Particle Accelerator Conference, Campinas (Brazil), 24 May 2021 - 28 May 2021.  
<https://bib-pubdb1.desy.de/record/472675>
- Biswas, S., Husek, J., Londo, S. & Baker, L. R. (2018). *The Journal of Physical Chemistry Letters*, **9**(17), 5047–5054. Publisher: American Chemical Society.  
<https://doi.org/10.1021/acs.jpcclett.8b01865>
- Brachmann, A., Dunham, M. & Schmerge, J. F. (2019). In *Proc. FEL'19*, Free Electron Laser Conference, pp. 772–775. JACoW Publishing, Geneva, Switzerland. ISSN: "" Issue: 39.  
<http://jacow.org/fel2019/papers/fra02.pdf>
- Carneiro, L. M., Cushing, S. K., Liu, C., Su, Y., Yang, P., Alivisatos, A. P. & Leone, S. R. (2017). *Nat Mater*, **16**(8), 819–825.
- Carva, K., Legut, D. & Oppeneer, P. M. (2009). *Europhysics Letters*, **86**(5), 57002.  
<https://dx.doi.org/10.1209/0295-5075/86/57002>
- Decking, W., Abeghyan, S., Abramian, P. *et al.* (2020). *Nature Photonics*, **14**(6), 391–397.
- Döring, F., Rösner, B., Langer, M., Kubec, A., Kleibert, A., Raabe, J., Vaz, C. A. F., Lebugle, M. & David, C. (2020). *Optica*, **7**(8), 1007–1014. Publisher: Optica Publishing Group.  
<https://opg.optica.org/optica/abstract.cfm?uri=optica-7-8-1007>
- Emma, P., Akre, R., Arthur, J., Bionta, R., Bostedt, C., Bozek, J., Brachmann, A., Bucksbaum, P., Coffee, R., Decker, F. J., Ding, Y., Dowell, D., Edstrom, S., Fisher, A., Frisch, J., Gilevich, S., Hastings, J., Hays, G., Hering, P., Huang, Z., Iverson, R., Loos, H., Messerschmidt, M., Miahnahri, A., Moeller, S., Nuhn, H. D., Pile, G., Ratner, D., Rzepiela, J., Schultz, D., Smith, T., Stefan, P., Tompkins, H., Turner, J., Welch, J., White, W., Wu, J., Yocky, G. & Galayda, J. (2010). *Nature Photonics*, **4**(9), 641–647.
- Eschenlohr, A. (2021). *J Phys Condens Matter*, **33**(1), 013001.
- Eschenlohr, A., Battiato, M., Maldonado, P., Pontius, N., Kachel, T., Holldack, K., Mitzner, R., Fohlisch, A., Oppeneer, P. M. & Stamm, C. (2013). *Nat Mater*, **12**(4), 332–6.
- Eschenlohr, A., Persichetti, L., Kachel, T., Gabureac, M., Gambardella, P. & Stamm, C. (2017). *J Phys Condens Matter*, **29**(38), 384002.
- Fangohr, H., Beg, M., Bergemann, M., Bondar, V., Brockhauser, S., Campbell, A., Carinan, C., Costa, R., Dall'Antonia, F., Danilevski, C., E, J., Ehsan, W., Esenov, S., Fabbri, R., Fangohr, S., Fernandez-del Castillo, E., Flucke, G., Fortmann-Grote, C., Fulla Marsa, D., Giovanetti, G., Goeries, D., Götz, A., Hall, J., Hauf, S., Hickin, D., Holm Rod, T., Jarosiewicz, T., Kamil, E., Karnevskiy, M., Kieffer, J., Kirienko, Y., Klimovskaia, A., Kluyver, T., Kuster, M., Le Guyader, L., Madsen, A., Maia, L., Mamchik, D., Mercadier, L., Michelat, T., Möller, J., Mohacsi, I., Parenti, A., Pellegrini, E., Perrin, J.-F., Reiser, M., Reppin, J., Rosca, R., Rück, D., Rüter, T., Santos, H., Schaffer, R., Scherz, A., Schlünzen, F., Scholz, M., Schuh, M., Selknaes, J. R., Silenzi, A., Sipsos, G., Spitzewski, M., Sztuk, J., Szuba, J., Taylor, J., Trojanowski, S., Wrona, K., Yaroslavtsev, A. & Zhu, J. (2020). pp. 799–806. JACOW Publishing, Geneva, Switzerland. ISSN: 2226-0358.  
<https://accelconf.web.cern.ch/icalpecs2019/doi/JACoW-ICALPECS2019-TUCPR02.html>
- Foglia, L., Vempati, S., Tanda Bonkano, B., Gierster, L., Wolf, M., Sadofev, S. & Stahler, J. (2019). *Struct Dyn*, **6**(3), 034501.
- Gerasimova, N., La Civita, D., Samoylova, L., Vannoni, M., Villanueva, R., Hickin, D., Carley, R., Gort, R., Van Kuiken, B. E., Miedema, P., Le Guyader, L., Mercadier, L., Mercurio, G., Schlappa, J., Teichman, M., Yaroslavtsev, A., Sinn, H. & Scherz, A. (2022). *J Synchrotron Radiat*, **29**(Pt 5), 1299–1308.

- Gillmeister, K., Golež, D., Chiang, C.-T., Bittner, N., Pavlyukh, Y., Berakdar, J., Werner, P. & Widdra, W. (2020). *Nature Communications*, **11**(1), 4095. Publisher: Nature Publishing Group.  
<https://www.nature.com/articles/s41467-020-17925-8>
- Hennecke, M., Radu, I., Abrudan, R., Kachel, T., Holldack, K., Mitzner, R., Tsukamoto, A. & Eisebitt, S. (2019). *Physical Review Letters*, **122**(15), 157202. Publisher: American Physical Society.  
<https://link.aps.org/doi/10.1103/PhysRevLett.122.157202>
- Holldack, K., Bahrtdt, J., Balzer, A., Bovensiepen, U., Brzhezinskaya, M., Erko, A., Eschenlohr, A., Follath, R., Firsov, A., Frentrup, W., Le Guyader, L., Kachel, T., Kuske, P., Mitzner, R., Muller, R., Pontius, N., Quast, T., Radu, I., Schmidt, J. S., Schussler-Langeheine, C., Sperling, M., Stamm, C., Trabant, C. & Fohlisch, A. (2014). *J Synchrotron Radiat*, **21**(Pt 5), 1090–104.
- Ishikawa, T., Aoyagi, H., Asaka, T., Asano, Y., Azumi, N., Bizen, T., Ego, H., Fukami, K., Fukui, T., Furukawa, Y., Goto, S., Hanaki, H., Hara, T., Hasegawa, T., Hatsui, T., Higashiya, A., Hirono, T., Hosoda, N., Ishii, M., Inagaki, T., Inubushi, Y., Itoga, T., Joti, Y., Kago, M., Kameshima, T., Kimura, H., Kirihara, Y., Kiyomichi, A., Kobayashi, T., Kondo, C., Kudo, T., Maesaka, H., Maréchal, X. M., Masuda, T., Matsubara, S., Matsumoto, T., Matsushita, T., Matsui, S., Nagasono, M., Nariyama, N., Ohashi, H., Ohata, T., Ohshima, T., Ono, S., Otake, Y., Saji, C., Sakurai, T., Sato, T., Sawada, K., Seike, T., Shirasawa, K., Sugimoto, T., Suzuki, S., Takahashi, S., Takebe, H., Takeshita, K., Tamasaku, K., Tanaka, H., Tanaka, R., Tanaka, T., Togashi, T., Togawa, K., Tokuhisa, A., Tomizawa, H., Tono, K., Wu, S., Yabashi, M., Yamaga, M., Yamashita, A., Yanagida, K., Zhang, C., Shintake, T., Kitamura, H. & Kumagai, N. (2012). *Nature Photonics*, **6**(8), 540–544.
- Kachel, T., Pontius, N., Stamm, C., Wietstruck, M., Aziz, E. F., Dürr, H. A., Eberhardt, W. & de Groot, F. M. F. (2009). *Physical Review B*, **80**(9), 092404. Publisher: American Physical Society.  
<https://link.aps.org/doi/10.1103/PhysRevB.80.092404>
- Ko, I. S., Kang, H.-S., Heo, H., Kim, C., Kim, G., Min, C.-K., Yang, H., Baek, S. Y., Choi, H.-J., Mun, G., Park, B. R., Suh, Y. J., Shin, D. C., Hu, J., Hong, J., Jung, S., Kim, S.-H., Kim, K., Na, D., Park, S. S., Park, Y. J., Jung, Y. G., Jeong, S. H., Lee, H. G., Lee, S., Lee, S., Oh, B., Suh, H. S., Han, J.-H., Kim, M. H., Jung, N.-S., Kim, Y.-C., Lee, M.-S., Lee, B.-H., Sung, C.-W., Mok, I.-S., Yang, J.-M., Parc, Y. W., Lee, W.-W., Lee, C.-S., Shin, H., Kim, J. H., Kim, Y., Lee, J. H., Park, S.-Y., Kim, J., Park, J., Eom, I., Rah, S., Kim, S., Nam, K. H., Park, J., Park, J., Kim, S., Kwon, S., An, R., Park, S. H., Kim, K. S., Hyun, H., Kim, S. N., Kim, S., Yu, C.-J., Kim, B.-S., Kang, T.-H., Kim, K.-W., Kim, S.-H., Lee, H.-S., Lee, H.-S., Park, K.-H., Koo, T.-Y., Kim, D.-E. & Lee, K. B. (2017). *Applied Sciences*, **7**(5), 479. Number: 5 Publisher: Multidisciplinary Digital Publishing Institute.  
<https://www.mdpi.com/2076-3417/7/5/479>
- Le Guyader, L., Eschenlohr, A., Beye, M., Schlotter, W., Doring, F., Carinan, C., Hickin, D., Agarwal, N., Boeglin, C., Bovensiepen, U., Buck, J., Carley, R., Castoldi, A., D'Elia, A., Delitz, J. T., Ehsan, W., Engel, R., Erdinger, F., Fangohr, H., Fischer, P., Fiorini, C., Fohlisch, A., Gelisio, L., Gensch, M., Gerasimova, N., Gort, R., Hansen, K., Hauf, S., Izquierdo, M., Jal, E., Kamil, E., Karabekyan, S., Kluyver, T., Laarmann, T., Lojewski, T., Lomidze, D., Maffessanti, S., Mamyrbayev, T., Marcelli, A., Mercadier, L., Mercurio, G., Miedema, P. S., Ollefs, K., Rossnagel, K., Rosner, B., Rothenbach, N., Samartsev, A., Schlappa, J., Setoodehnia, K., Sorin Chiuzbaian, G., Spieker, L., Stamm, C., Stellato, F., Techert, S., Teichmann, M., Turcato, M., Van Kuiken, B., Wende, H., Yaroslavtsev, A., Zhu, J., Molodtsov, S., David, C., Porro, M. & Scherz, A. (2023). *J Synchrotron Radiat*, **30**(Pt 2), 284–300.
- Lojewski, T., Elhanoty, M. F., Le Guyader, L., Grånäs, O., Agarwal, N., Boeglin, C., Carley, R., Castoldi, A., David, C., Deiter, C., Döring, F., Engel, R., Erdinger, F., Fangohr, H., Fiorini, C., Fischer, P., Gerasimova, N., Gort, R., deGroot, F., Hansen, K., Hauf, S., Hickin, D., Izquierdo, M., Van Kuiken, B. E., Kvashnin, Y., Lambert, C.-H., Lomidze, D., Maffessanti, S., Mercadier, L., Mercurio, G., Miedema, P. S., Ollefs, K., Pace, M., Porro, M., Rezvani, J., Rösner, B., Rothenbach, N., Samartsev, A., Scherz, A., Schlappa, J., Stamm, C., Teichmann, M., Thunström, P., Turcato, M., Yaroslavtsev, A., Zhu, J., Beye, M., Wende, H., Bovensiepen, U., Eriksson, O. & Eschenlohr, A. (2023). *Materials Research Letters*, **11**(8), 655–661.

- Lojewski, T., Elhanoty, M. F., Le Guyader, L., Grånäs, O., Agarwal, N., Boeglin, C., Carley, R., Castoldi, A., David, C., Deiter, C., Döring, F., Engel, R., Erdinger, F., Fangohr, H., Fiorini, C., Fischer, P., Gerasimova, N., Gort, R., deGroot, F., Hansen, K., Hauf, S., Hickin, D., Izquierdo, M., Van Kuiken, B. E., Kvashnin, Y., Lambert, C.-H., Lomidze, D., Maffessanti, S., Mercadier, L., Mercurio, G., Miedema, P. S., Ollefs, K., Pace, M., Porro, M., Rezvani, J., Rösner, B., Rothenbach, N., Samartsev, A., Scherz, A., Schlappa, J., Stamm, C., Teichmann, M., Thunström, P., Turcato, M., Yaroslavtsev, A., Zhu, J., Beye, M., Wende, H., Bovensiepen, U., Eriksson, O. & Eschenlohr, A., (2020). Data recorded in the experiments on ni-metal at the european xfel are available at doi: 10.22003/xfel.eu-data-002161-00.
- Lojewski, T., Golez, D., Ollefs, K., Guyader, L. L., Kämmerer, L., Rothenbach, N., Engel, R. Y., Miedema, P. S., Beye, M., Chiuzbăian, G. S., Carley, R., Gort, R., Van Kuiken, B. E., Mercurio, G., Schlappa, J., Yaroslavtsev, A., Scherz, A., Döring, F., David, C., Wende, H., Bovensiepen, U., Eckstein, M., Werner, P. & Eschenlohr, A., (2021). Data recorded in the experiments on nio at the european xfel are available at doi: 10.22003/xfel.eu-data-002589-00.
- Lojewski, T., Golez, D., Ollefs, K., Guyader, L. L., Kämmerer, L., Rothenbach, N., Engel, R. Y., Miedema, P. S., Beye, M., Chiuzbăian, G. S., Carley, R., Gort, R., Van Kuiken, B. E., Mercurio, G., Schlappa, J., Yaroslavtsev, A., Scherz, A., Döring, F., David, C., Wende, H., Bovensiepen, U., Eckstein, M., Werner, P. & Eschenlohr, A., (2024). Photo-induced charge-transfer renormalization in NiO. ArXiv:2305.10145 [cond-mat]. <http://arxiv.org/abs/2305.10145>
- López-Flores, V., Arabski, J., Stamm, C., Halté, V., Pontius, N., Beaufrepaire, E. & Boeglin, C. (2012). *Physical Review B*, **86**(1), 014424. Publisher: American Physical Society. <https://link.aps.org/doi/10.1103/PhysRevB.86.014424>
- López-Flores, V., Berggaard, N., Halté, V., Stamm, C., Pontius, N., Hehn, M., Otero, E., Beaufrepaire, E. & Boeglin, C. (2013). *Physical Review B*, **87**(21), 214412. Publisher: American Physical Society. <https://link.aps.org/doi/10.1103/PhysRevB.87.214412>
- Patterson, B. D., Abela, R., Braun, H.-H., Flechsig, U., Ganter, R., Kim, Y., Kirk, E., Oppelt, A., Pedrozzi, M., Reiche, S., Rivkin, L., Schmidt, T., Schmitt, B., Strocov, V. N., Tsujino, S. & Wrulich, A. F. (2010). *New Journal of Physics*, **12**(3), 035012. <https://dx.doi.org/10.1088/1367-2630/12/3/035012>
- Pergament, M., Palmer, G., Kellert, M., Kruse, K., Wang, J., Wissmann, L., Wegner, U., Emons, M., Kane, D., Priebe, G., Venkatesan, S., Jezynski, T., Pallas, F. & Lederer, M. J. (2016). *Optics Express*, **24**(26), 29349–29359.
- Porro, M., Andricek, L., Aschauer, S., Castoldi, A., Donato, M., Engelke, J., Erdinger, F., Fiorini, C., Fischer, P., Graafsma, H., Grande, A., Guazzoni, C., Hansen, K., Hauf, S., Kalavakuru, P., Klaer, H., Tangl, M., Kugel, A., Kuster, M., Lechner, P., Lomidze, D., Maffessanti, S., Manghisoni, M., Nidhi, S., Okrent, F., Re, V., Reckleben, C., Riceputi, E., Richter, R., Samartsev, A., Schlee, S., Soldat, J., Strüder, L., Szymanski, J., Turcato, M., Weidenspointner, G. & Wunderer, C. B. (2021). *IEEE Transactions on Nuclear Science*, **68**(6), 1334–1350. Conference Name: IEEE Transactions on Nuclear Science. <https://ieeexplore.ieee.org/document/9419081>
- Raubenheimer, T. O. (2018). In *Proc. 60th ICFA Advanced Beam Dynamics Workshop (FLS'18), Shanghai, China, 5-9 March 2018*, ICFA Advanced Beam Dynamics Workshop, pp. 6–11. Geneva, Switzerland: JACoW Publishing. Issue: 60. <http://jacow.org/fls2018/papers/mop1wa02.pdf>
- Rothenbach, N., Gruner, M. E., Ollefs, K., Schmitz-Antoniak, C., Salamon, S., Zhou, P., Li, R., Mo, M., Park, S., Shen, X., Weathersby, S., Yang, J., Wang, X. J., Pentcheva, R., Wende, H., Bovensiepen, U., Sokolowski-Tinten, K. & Eschenlohr, A. (2019). *Physical Review B*, **100**(17), 174301. Publisher: American Physical Society. <https://link.aps.org/doi/10.1103/PhysRevB.100.174301>
- Rothenbach, N., Gruner, M. E., Ollefs, K., Schmitz-Antoniak, C., Salamon, S., Zhou, P., Li, R., Mo, M., Park, S., Shen, X., Weathersby, S., Yang, J., Wang, X. J., Šipr, O., Ebert, H., Sokolowski-Tinten, K., Pentcheva, R., Bovensiepen, U., Eschenlohr, A. & Wende, H. (2021). *Physical Review B*, **104**(14), 144302. Publisher: American Physical Society. <https://link.aps.org/doi/10.1103/PhysRevB.104.144302>

- Santomauro, F. G., Grilj, J., Mewes, L., Nedelcu, G., Yakunin, S., Rossi, T., Capano, G., Al Haddad, A., Budarz, J., Kinschel, D., Ferreira, D. S., Rossi, G., Gutierrez Tovar, M., Grolimund, D., Samson, V., Nachttegaal, M., Smolentsev, G., Kovalenko, M. V. & Chergui, M. (2016). *Structural Dynamics*, **4**(4), 044002.  
<https://doi.org/10.1063/1.4971999>
- SCS-team, (2024). SCS / ToolBox · GitLab.  
<https://git.xfel.eu/SCS/ToolBox>
- Stamm, C., Kachel, T., Pontius, N., Mitzner, R., Quast, T., Holldack, K., Khan, S., Lupulescu, C., Aziz, E. F., Wietstruk, M., Durr, H. A. & Eberhardt, W. (2007). *Nat Mater*, **6**(10), 740–3.
- Stamm, C., Murer, C., Wörnle, M. S., Acremann, Y., Gort, R., Däster, S., Reid, A. H., Higley, D. J., Wandel, S. F., Schlotter, W. F. & Gambardella, P. (2020). *Journal of Applied Physics*, **127**(22), 223902.  
<https://doi.org/10.1063/5.0006095>
- Stamm, C., Pontius, N., Kachel, T., Wietstruk, M. & Dürr, H. A. (2010). *Physical Review B*, **81**(10), 104425. Publisher: American Physical Society.  
<https://link.aps.org/doi/10.1103/PhysRevB.81.104425>
- Stepanov, A. G. & Hauri, C. P. (2016). *J Synchrotron Radiat*, **23**(1), 141–51.
- Stöhr, J. & Siegmann, H. C. (2006). *Magnetism*. Berlin, Heidelberg: Springer.  
<http://link.springer.com/10.1007/978-3-540-30283-4>
- Tschentscher, T., Bressler, C., Grünert, J., Madsen, A., Mancuso, A. P., Meyer, M., Scherz, A., Sinn, H. & Zastra, U. (2017). *Applied Sciences*, **7**(6), 592. Number: 6 Publisher: Multidisciplinary Digital Publishing Institute.  
<https://www.mdpi.com/2076-3417/7/6/592>
- Uemura, Y., Ismail, A. S. M., Park, S. H., Kwon, S., Kim, M., Elnaggar, H., Frati, F., Wadati, H., Hirata, Y., Zhang, Y., Yamagami, K., Yamamoto, S., Matsuda, I., Halisdemir, U., Koster, G., Milne, C., Ammann, M., Weckhuysen, B. M. & Groot, F. M. F. d. (2022). *Journal of Physical Chemistry Letters*, **13**(19), 4207–4214. Publisher: American Chemical Society.  
<https://tohoku.elsevierpure.com/en/publications/hole-dynamics-in-photoexcited-hematite-studied-with-femtosecond-o>
- Uemura, Y., Ismail, A. S. M., Park, S. H., Kwon, S., Kim, M., Niwa, Y., Wadati, H., Elnaggar, H., Frati, F., Haerman, T., Höppel, N., Huse, N., Hirata, Y., Zhang, Y., Yamagami, K., Yamamoto, S., Matsuda, I., Katayama, T., Togashi, T., Owada, S., Yabashi, M., Halisdemir, U., Koster, G., Yokoyama, T., Weckhuysen, B. M. & de Groot, F. M. F. (2021). *The Journal of Physical Chemistry C*, **125**(13), 7329–7336. Publisher: American Chemical Society.  
<https://doi.org/10.1021/acs.jpcc.0c10525>
- Wang, H., Friedrich, S., Li, L., Mao, Z., Ge, P., Balasubramanian, M. & S. Patil, D. (2018). *Physical Chemistry Chemical Physics*, **20**(12), 8166–8176. Publisher: Royal Society of Chemistry.  
<https://pubs.rsc.org/en/content/articlelanding/2018/cp/c7cp06624d>
- Willmott, P. (2019). *An Introduction to Synchrotron Radiation: Techniques and Applications*. John Wiley & Sons, Ltd. eprint:  
<https://onlinelibrary.wiley.com/doi/epub/10.1002/9781119280453>  
<https://doi.org/10.1002/9781119280453>
- Yu, J., Rosso, K. M. & Bruemmer, S. M. (2012). *The Journal of Physical Chemistry C*, **116**(2), 1948–1954. Publisher: American Chemical Society.  
<https://doi.org/10.1021/jp208080v>
- Zhang, H., Debroye, E., Vina-Bausa, B., Valli, D., Fu, S., Zheng, W., Di Virgilio, L., Gao, L., Frost, J. M., Walsh, A., Hofkens, J., Wang, H. I. & Bonn, M. (2023). *ACS Energy Lett*, **8**(1), 420–428.

iucr

---

**Synopsis**

We disentangle and analyze the secondary contribution of long-lived excitations that occur in high-repetition-rate stroboscopic X-ray absorption spectroscopy experiments of Ni and NiO thin film samples.

---